2022

Modeling the formation of efflorescence and subflorescence caused by salt solution evaporation from porous media

Rishav Roy

Justin Weibel
jaweibel@purdue.edu

Suresh V. Garimella

Roy, Rishav; Weibel, Justin; and Garimella, Suresh V., "Modeling the formation of efflorescence and subflorescence caused by salt solution evaporation from porous media" (2022). *CTRC Research Publications.* Paper 392.
http://dx.doi.org/10.1115/1.4054263

Modeling the Formation of Efflorescence and Subflorescence Caused by Salt Solution Evaporation from Porous Media

Rishav Roy, Justin A. Weibel*, Suresh V. Garimella

School of Mechanical Engineering and Birck Nanotechnology Center

Purdue University, West Lafayette, Indiana 47907 USA

ABSTRACT

Understanding the dynamics of precipitation and crystallization as salt solutions evaporate from porous media is of importance in the context of preservation of historical monuments, understanding soil nutrient content, and design of porous evaporators for use in distillation plants. Transient advection-diffusion equations govern the salt mass fraction profile of the solution inside the porous medium. These governing equations are solved to obtain the solute mass fraction profile within the porous medium as well as the effloresced salt crust. Further accounting for precipitation allows a study of the formation and growth of efflorescence and subflorescence. Crystallization experiments are performed by allowing a NaCl solution to evaporate from a porous medium of copper particles and the subflorescence trends predicted by the model are validated. The modeling framework offers a comprehensive tool for predicting the spatio-temporal solute mass fraction profiles and subsequent precipitation in a porous medium.

Keywords: porous media; efflorescence; subflorescence; solute transport; evaporation

1 INTRODUCTION

Evaporation of salt solutions from porous media often leads to the formation of salt crystals either inside the medium or on its surface. Driven by evaporation, the mass fraction of the salt solution increases over time and crystals form when the local saturation (defined as the ratio of the local ion mass fraction to the equilibrium ion mass fraction) reaches critical supersaturation. When the crystals form on the surface of a porous medium it is referred to as efflorescence, and if formed inside the medium it is referred to as subflorescence [1]. Efflorescence formed on the outside of the medium does not influence its internal structural integrity. On the other hand, subflorescence blocks the internal pores and often proves detrimental to the structural integrity of the medium [2–4]. It is important to understand the effects of salt content and crystallization in the context of preserving buildings and historical monuments [5–7] and understanding the nutrient profile of soil [8–10]. Modulating the process of solute transport driven by evaporation has applications in the production of catalysts [11,12]. Understanding evaporation of salt solutions from porous media can also be important for applications in distillation plants. Porous evaporators are well-known for their high efficiency of energy conversion from solar insolation to steam generation [13–15]. Utilizing porous evaporators in distillation processes, such as in multi-effect distillation (MED) plants [16,17], can improve the thermal efficiency of the plant as well as reduce the overall size by potentially reducing the number of distillation stages. Use of novel porous materials has also been proposed to enhance the efficiency of solar desalination [18–22] and in distillation units of ocean thermal energy conversion (OTEC) plants [23]. However, such evaporators typically handle high saline mass fractions and will have an associated risk of subflorescence occurring inside the porous evaporator medium, leading to eventual failure. It is thus necessary to understand the dynamics of salt crystallization and how it depends on parameters such as evaporation flux, saline mass fraction, and medium pore size.

Several aspects of these crystallization dynamics have been investigated. The formation of efflorescence [8,24] and its impact on the evaporation rate [25] has been examined experimentally. A few

efforts have focused on examining the efflorescence pattern due to heterogeneities in the constituent particle size [26–29]. Subflorescence in the medium has been observed using optical imaging [25,30] or x-ray microtomography [31,32]. Several studies have developed theoretical models and utilized numerical methods to evaluate the mass fraction profile of salt ions within a porous medium during evaporation of a salt solution. Transient advection-diffusion equations for transport in porous media are the most commonly solved governing equations. These equations follow the standard equations for continuum modeling of macro-scale transport with a consideration of the porosity, but ignore pore-scale dynamics. Some calculate the mass fraction profile inside the porous medium during the initial stage of evaporation preceding the occurrence of any precipitation [8,31,33], and as such, cannot be applied to the evaporation process once crystallization initiates. A few investigations include the effects of precipitation and dissolution by considering a reaction term [24,34], but they are limited to the evaluation of the mass fraction profile within an effloresced salt precipitate and do not predict the occurrence of subflorescence. Yet other approaches utilize pore-network model simulations [26,27,35,36] which model the void volume as a network of cylindrical throats connecting the pores. Pore-scale simulations, although computationally expensive, are a useful tool to understand solute transport at the microscale. However, these studies also focus only on the dynamics of the evaporation process prior to crystallization. There is a need for a modeling approach which can evaluate solute transport inside the porous medium before and after the onset of crystallization, and hence predict the formation and subsequent growth of efflorescence and subflorescence. The predictive capabilities of the existing models in the literature are summarized in Table 1.

The present work considers a porous medium filled with salt solution that is subjected to evaporation at the top surface and continually replenished from below by a saline source at a fixed mass fraction. A numerical solution of the macroscale transient advection-diffusion equation yields the mass fraction profile within the porous medium. The processes of precipitation and dissolution are also considered by the inclusion of a reaction term. This consequently imparts the capability of predicting the growth of

efflorescence on the surface of the medium and the subsequent solute transport through the porous effloresced structure as well. The amount of subflorescence within the medium is also predicted as a result of the inclusion of the reaction term. The dependence of the efflorescence and subflorescence trends on the evaporation flux and the mass fraction of the saline solution source are investigated. To the best of our knowledge, such a comprehensive predictive analysis, considering all transport processes occurring inside the porous medium and the effloresced salt structure, has not yet been done. We also perform a series of experiments to replicate these behaviors predicted by the numerical solution, and in particular, demonstrate that crystallization can be prevented by controlling the operating conditions and the amount of subflorescence can be controlled if crystallization does occur. The advantages of the modeling framework we present in this study in comparison to those in the literature are summarized in Table 1.

Table 1. Summary of the existing models in the literature to study solute transport through a porous medium, and a comparison with the modeling framework presented in the current work.

Prediction capability/characteristic		**Existing models in the literature**			**Presented modeling framework**
		Advection-diffusion equation [8,31,33]	**Precipitation-dissolution equation** [24,34]	**Pore-network model** [26,27,35,36]	
Onset of crystallization		Yes	No	Yes	Yes
Mass fraction profile in:	**Porous medium**	Yes	No	Yes	Yes
	Effloresced salt	No	Yes	No	Yes
Efflorescence growth		No	Yes	No	Yes
Subflorescence growth		No	No	No	Yes
Pore-scale dynamics		No	No	Yes	No
Computational expense		Low	Low	High	Low

2 MODELING APPROACH AND PREDICTIONS

The process of evaporation-driven wicking of a solution of sodium chloride (NaCl) through a porous medium is considered in our work. NaCl has been chosen as the salt of interest owing to its abundance in seawater and its consequent widespread presence in distillation plants. The porous medium properties are represented as spherical copper particles to facilitate a comparison with our experiments (described later in Section 3). However, the modeling approach is not restricted to these material choices. The model considers the one-dimensional domain shown in Figure 1 in which a source of NaCl solution (at fixed mass fraction) feeds the porous medium from below while water evaporates from the top that is open to an ambient. Equations describing the advection and diffusion of NaCl through the porous medium are solved numerically to obtain the spatial and temporal variations of NaCl mass fraction. Precipitation in the form of efflorescence as well as subflorescence is then predicted. The boundary conditions and the coordinate system employed in the governing equations are shown in Figure 1. A second domain above the porous medium represents the porous effloresced salt crust, and is added to the governing equations only once efflorescence starts. The coordinate along the length of the channel is z and the subscripts p and s refer to the values corresponding to the porous domain and the salt crust domain, respectively. The length of the porous medium domain, L_p, is taken as 20 mm and L_s is the salt crust length, which is computed while solving the equations.

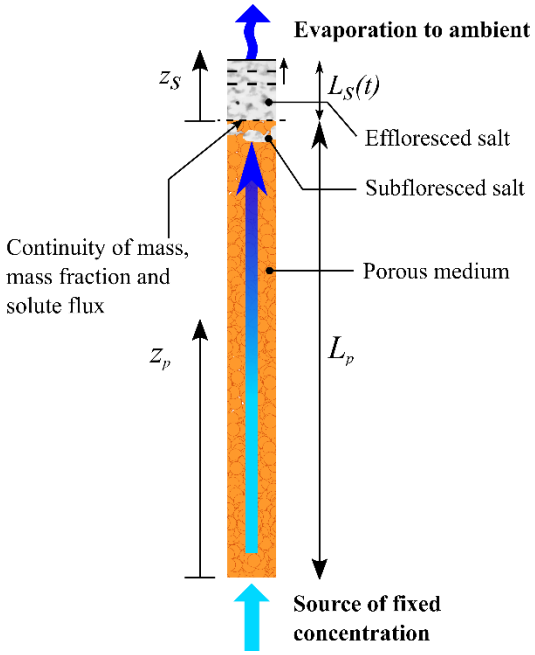

Figure 1. Schematic diagram of the one-dimensional solution domain showing the source of salt solution, the porous medium, the subfloresced salt below the top surface of the porous medium, and the effloresced salt on top of the porous medium. The associated boundary conditions and coordinate systems are shown alongside the zones. [1 column wide]

2.1 Governing Equations

The transport of salt through the porous medium is described by the following 1D transient advection-diffusion equation:

$$\frac{\partial}{\partial t}\left(\rho\varepsilon_p w_p\right)+\frac{\partial}{\partial z_p}\left(\rho\varepsilon_p U_p w_p\right)=\frac{\partial}{\partial z_p}\left(\rho\varepsilon_p D_p^{*}\frac{\partial w_p}{\partial z_p}\right) \quad (1)$$

where ρ is the density of the salt solution assumed to be 1000 kg/m^3, ε_p is the porous domain porosity taken as 0.65, w_p is the mass fraction of NaCl (g of NaCl/g of solution), U_p is the interstitial velocity of the solution through the medium, and $D_p^{*}=D\varepsilon_p^{0.33}$ is the effective diffusion coefficient of NaCl in water.

Here D = 1.3×10^{-9} m^2/s [34] and the factor $\varepsilon_p^{0.33}$ accounts for the effects of tortuosity [37]. The density, porosity, and diffusion coefficient are held constant in the domain.

The salt solution wicks into the medium at $z_p = 0$ from an infinite source of mass fraction w_0. This is represented by the boundary condition:

$$w_p(z_p = 0, t) = w_0 \tag{2}$$

Water evaporates from the top surface at $z_p = L_p$ that is exposed to the ambient air. There must be a balance between the advective and diffusive fluxes of NaCl at the top surface because the salt cannot escape into the ambient air. This is expressed in the boundary condition:

$$\rho\varepsilon_p U_p w_p(z_p = L_p, t) - \rho\varepsilon_p D_p^* \left.\frac{\partial w_p}{\partial z_p}\right|_{z_p = L_p} = 0 \tag{3}$$

The interstitial velocity of the solution inside the medium is calculated from the evaporation flux at the top surface and remains invariant throughout the medium

$$U_p = \frac{j''}{\rho\varepsilon_p} \tag{4}$$

The pores are assumed to be filled with the salt solution from the source at the start of the process and thus the initial condition is

$$w_p\left(z_p, t = 0\right) = w_0 \tag{5}$$

If the source mass fraction $w_0 < 1$, this implies that the solution is undersaturated everywhere within the medium initially. The mass fraction, and equivalently the saturation (defined as $S = w/w_{sat}$ where w_{sat} is the equilibrium ion mass fraction and is equal to 0.264 for NaCl in water [24,34]), increases within the medium in time because evaporation depletes water and leaves behind salt ions which accumulate in the medium. Steady state is achieved when ion transport by diffusion balances ion transport by advection.

Crystallization will initiate if and when the local saturation at any location reaches the critical supersaturation (denoted by S_{crit} and taken as 1.6 [38]). However, when advection of ions is weak (due to a low evaporation rate), crystallization will never occur if the steady state is achieved with a mass fraction profile below the critical supersaturation throughout the domain. Hence, we first analyze the mass fraction profile at steady state.

2.2 Steady-State Analysis

The transient term in equation (1) vanishes at steady state. The equation can be non-dimensionalized by taking $\bar{z}_p = z_p / L_p$ and reduces to the following form

$$Pe \frac{\partial w_p}{\partial \bar{z}_p} = \frac{\partial^2 w_p}{\partial \bar{z}_p^2} \tag{6}$$

The mass fraction profile within the medium is dictated by the Péclet number defined as $Pe = U_p L_p / D_p^*$, the ratio of ion transport by advection to that by diffusion. Equation (6) is solved for the steady-state mass fraction profile $w_p(\bar{z}_p) = w_0 \exp\left(\mathrm{Pe}\, \bar{z}_p\right)$, where the maximum mass fraction of NaCl within the medium occurs at the top surface, $w_p\left(\bar{z}_p = 1\right) = w_0 \exp(\mathrm{Pe})$. A low *Pe* resulting from a relatively low evaporation flux can prevent the maximum mass fraction within the medium from exceeding the critical supersaturation value S_{crit}, consequently preventing any crystallization. On the contrary, if *Pe* is high due to a higher evaporation flux, the local saturation can exceed S_{crit}. In such a situation, efflorescence and subflorescence can occur. Equating the maximum steady-state mass fraction to the value at critical supersaturation, $w_0 exp(Pe) = S_{crit} w_{sat}$, gives the threshold *Pe* number beyond which crystallization will occur:

$$Pe = \log\left(\frac{S_{crit}}{S_0}\right) \tag{7}$$

where $S_0 = w_0 / w_{sat}$ is the saturation of the NaCl source.

2.3 After the Onset of Crystallization

Crystallization in the form of efflorescence and subflorescence occurs if *Pe* exceeds the threshold value given in equation (7). Once the critical supersaturation is exceeded and crystallization initiates, the governing equation and the boundary conditions change due to precipitation/dissolution of NaCl in the medium. A crust of NaCl grows on the top of the porous medium as efflorescence and simultaneously precipitation occurs within the medium close to $z_p = L_p$, leading to subflorescence. Two distinct domains are analyzed: i) the porous medium domain and ii) the effloresced salt crust domain. As shown in Figure 1 a different coordinate variable z_s is defined for the salt crust domain. The porous domain is represented by z_p which varies from 0 to L_p while z_s varies from 0 to L_s; $z_p = L_p$ is coincident with $z_s = 0$. The equation governing the transport of salt in both zones is:

$$\rho\varepsilon_i \frac{\partial w_i}{\partial t} + \rho\varepsilon_i U_i \frac{\partial w_i}{\partial z_i} = \frac{\partial}{\partial z_i}\left(\rho\varepsilon_i D_i^* \frac{\partial w_i}{\partial z_i} \right) - a_v \rho k_r \left(w_i - w_{sat} \right) \tag{8}$$

The subscript *i* can be either *p* or *s* to represent the properties of the porous medium or the salt crust domains, respectively. As discussed above in Section 2.1, $D_i^* = D\varepsilon_i^{0.33}$. It is important to note that once critical supersaturation is exceeded, secondary nucleation occurs at a saturation value of 1. This is implicitly indicated in the reaction term in equation (8) where the driving force for precipitation is proportional to $(w_i - w_{sat})$. Equation (8) also has an inherent assumption of spatially invariant velocity along the domain length. This assumption and the associated implications on the solution accuracy, are discussed in detail in Section S1 of the Supporting Information. The additional term on the right side of equation (8) accounts for precipitation/dissolution of salt in the medium, where $a_v = \frac{3(1-\varepsilon)}{r_b}$ [34] is the pore surface area per unit volume and k_r is the reaction coefficient. Widely varying values of the reaction coefficient have been reported in the literature, from O(μm/s) [39] to O(mm/s) [34]. The wide range of values reported necessitated a sensitivity analysis which is discussed in detail in Section S4 of the Supporting Information. In this study, we have taken the reaction coefficient as 1 μm/s. The pore radius

r_b is estimated as $r_b = 0.21D_p$ for a sintered copper powder wick [40], where D_p is the copper particle diameter taken as 200 μm to imitate the experimental conditions described later in Section 3. It is important to note that the additional reaction term is locally activated in the porous domain only once the local saturation exceeds critical supersaturation. For the salt crust domain, however, the reaction term is always active because the local saturation must have exceeded S_{crit} for the domain to exist. The boundary condition for the porous domain at $z_p = 0$ remain unchanged, as given by equation (2). The boundary condition at the top of the salt crust domain is obtained by modifying equation (3) to account for the growth of salt [34]:

$$\rho\varepsilon_s U_s\, w_s\big|_{z_s=L_s} - \rho\varepsilon_s D_s^* \left.\frac{\partial w_s}{\partial z_s}\right|_{z_s=L_s} = \left(\rho\varepsilon_s w_s + \left(1-\varepsilon_s\right)\rho_{cr}\right)\frac{dL_s}{dt} \tag{9}$$

where ρ_{cr} is the NaCl crystal density equal to 1.8 g/cm^3 and the subscript s refers to properties corresponding to the salt crust domain. A wide range of numbers have been reported for the salt crust porosity from 0.1 [34] to 0.43 [8] and a value of 0.4 is taken in this study. The sensitivity analysis discussed in Section S4 of the Supporting Information studies the impact of varying salt crust porosity. The interstitial velocity U_s is obtained by performing mass balance at the top surface $z_s = L_s$ of the salt crust:

$$\rho\varepsilon_s U_s = j'' + \left(\rho\varepsilon_s + \rho_{cr}\left(1-\varepsilon_s\right)\right)\frac{dL_s}{dt} \tag{10}$$

The two domains are coupled by equations for equality of mass fraction (equation (11)) and solute flux (equation (12)), and continuity equation at the boundary between the two domains (equation (13)):

$$w_p(z = L_p, t) = w_s(z_s = 0, t) \tag{11}$$

$$\rho\varepsilon_p U_p w_p\big|_{z_p=L_p} - \rho\varepsilon_p D_p^* \left.\frac{\partial w_p}{\partial z_p}\right|_{z_p=L_p} = \rho\varepsilon_s U_s w_s\big|_{z_s=0} - \rho\varepsilon_s D_s^* \left.\frac{\partial w_s}{\partial z_s}\right|_{z_s=0} \tag{12}$$

$$\rho \varepsilon_p U_p = \rho \varepsilon_s U_s \tag{13}$$

Using equations (11) and (13), equation (12) can be simplified to

$$\varepsilon_p D_p^* \left. \frac{\partial w_p}{\partial z_p} \right|_{z_p = L_p} = \varepsilon_s D_s^* \left. \frac{\partial w_s}{\partial z_s} \right|_{z_s = 0} \tag{14}$$

The evaporation rate is assumed to be constant throughout the simulated time. However, it can vary because of changing ambient conditions and suppression of vapor pressure due to the presence of a solute. A comprehensive analysis would include evaluation of evaporation rate based on other such considerations. Modeling the evaporation rate, however, is beyond the scope of this work but once determined, a dynamically changing evaporation rate can be incorporated into the model by simply plugging it into the boundary condition represented in equation (10). It should also be noted that the flow velocity in the porous medium and the effloresced salt crust are not constants but change dynamically. This dynamic behavior is captured by equation (10) which predicts the flow velocity in the salt crust and subsequently the flow velocity in the porous medium is calculated using equation (13).

2.4 Numerical Solution

An explicit finite-difference method (FDM) is utilized to solve the equations. Spatial gradients are approximated by second-order central difference schemes while the temporal gradients are approximated by a first-order forward difference scheme, resulting in an explicit method. Starting from the initial condition given by equation (5) and using the discretized forms of equation (1), and the boundary condition equations (2) and (3), we solve for the mass fraction inside the porous domain and march forward in time till the saturation at $z_p = L_p$ reaches critical supersaturation. Beyond this time, equations (8) and the corresponding boundary condition equations (9)-(13) need to be solved numerically in both the domains. The solutions of equations (1) and (8) are hereafter referred to as pre-crystallization and post-crystallization calculations, respectively. Implementing FDM on the salt crust domain is not trivial because the domain length changes over time. To overcome this issue, the governing equation is

modified by transforming the coordinates, $(z_s,t)\rightarrow(\tilde{z}_s,t)$ where $\tilde{z}_s = z_s / L_s(t)$, such that the salt crust length is normalized to 1 at all times. This coordinate transformation changes equation (8) to

$$\rho\varepsilon_s\frac{\partial\zeta}{\partial t}+\rho\varepsilon_s\left(\frac{U_s}{L_s(t)}-\frac{\tilde{z}_s}{L_s(t)}\frac{dL_s}{dt}\right)\frac{\partial\zeta}{\partial\tilde{z}_s}=\frac{\rho\varepsilon_s D_s^*}{L_s^2(t)}\frac{\partial^2\zeta}{\partial\tilde{z}_s^2}-a_v\rho k_r\left(\zeta-w_{sat}\right) \tag{15}$$

where $\zeta(\tilde{z}_s,t)$ is the mass fraction in the salt crust domain as a function of the transformed variables.

The FDM numerical scheme imposes constraints on the spatial and temporal discretizations to avoid numerical instabilities as described in detail in Section S2 of the Supporting Information. These constraints impose unrealistic bounds for time discretization (Δt ~ O(10^{-10} s)) while solving for the salt crust domain soon after the onset of crystallization. To circumvent this issue, equation (15) is solved for the salt crust domain with a quasi-steady state assumption till the crust length reaches a threshold value (L_s = 10^{-4} m) beyond which the constraint on time discretization relaxes (Δt ~ O(10^{-2} s)) and the explicit FDM is used to solve the equation. The explicit FDM and the quasi-steady state solution are respectively described in Sections S2 and S3 of the Supporting Information.

The amount of salt precipitated outside the medium (efflorescence) is calculated at the end of each time step. The increase in the amount of efflorescence is calculated by integrating the reaction term over the length of the salt crust domain and over a small period of time.

$$\int_{t_n}^{t_n+\Delta t}\int_0^{L_s(t)}a_v k_r\rho\left(w_s-w_{sat}\right)dz_s dt \tag{16}$$

The increase is reflected in the growth rate of the domain length which, in turn, gives the added length of the salt crust for the next time step.

$$\frac{dL_s(t)}{dt}=\frac{a_v k_r\rho\int_0^{L_s(t)}\left(w_s-w_{sat}\right)dz_s}{\left(1-\varepsilon_s\right)\rho_{cr}} \tag{17}$$

The calculations then continue for a user-defined length of time, set as 24 hr in this study.

The amount of salt precipitated inside the medium, which is a direct measure of the amount of subflorescence, can be calculated at each instant from the mass fraction profile inside the porous medium domain. A precipitate measure, *p*, is defined as the amount of local precipitation per unit cross-sectional area at a point inside the porous domain. It is calculated by integrating the reaction term from equation (8) over a differential length

$$p\left(z_p,t\right)=a_v k_r \rho\left(w_p(z_p,t)-w_{sat}\right)\Delta z_p \tag{18}$$

where Δz_p is the spatial discretization employed in the FDM. The total precipitation per unit cross-sectional area within the medium, *P*, over a period of time (*t = 0* to *t = T*) is calculated as

$$P(T)=\int_0^T\int_0^{L_p} a_v k_r \rho\left(w_p-w_{sat}\right)dzdt \tag{19}$$

It is worth noting that the model assumes that precipitation inside the domain does not affect the medium porosity which is reasonable for the low precipitation amounts observed, O(10^{-7} g/mm^2). If the amount of subflorescence became comparable to the pore volume (e.g., it is estimated that precipitation on the order of 10^{-5} g/mm^2 would be required to reduce porosity by ~10 %), then pore-blocking and consequent reduction in porosity would need to be accounted for while solving the equations. Pore-blocking due to subflorescence is expected to be more prominent for cases where a porous medium is drying, which is fundamentally different from the case we have considered. In our case, the evaporation front remains at the top surface as it is continuously fed by the salt solution from the bottom; hence, precipitation will be in the form of both efflorescence and subflorescence. For a drying porous medium, however, once the evaporation front recedes into the medium, precipitation would occur solely as subflorescence which would have led to pore-blocking.

2.5 Model Predictions

The evaporation flux, *j"*, and the source mass fraction, w_0, are the two input parameters varied in the simulations performed. The simulated period of time is 24 hr. A representative simulation result

corresponding to a source mass fraction of 0.2376 (S = 0.9) and an evaporation flux of 1.3×10^{-4} kg/m^{2}s (Pe = 3.55) is shown in Figure 2.

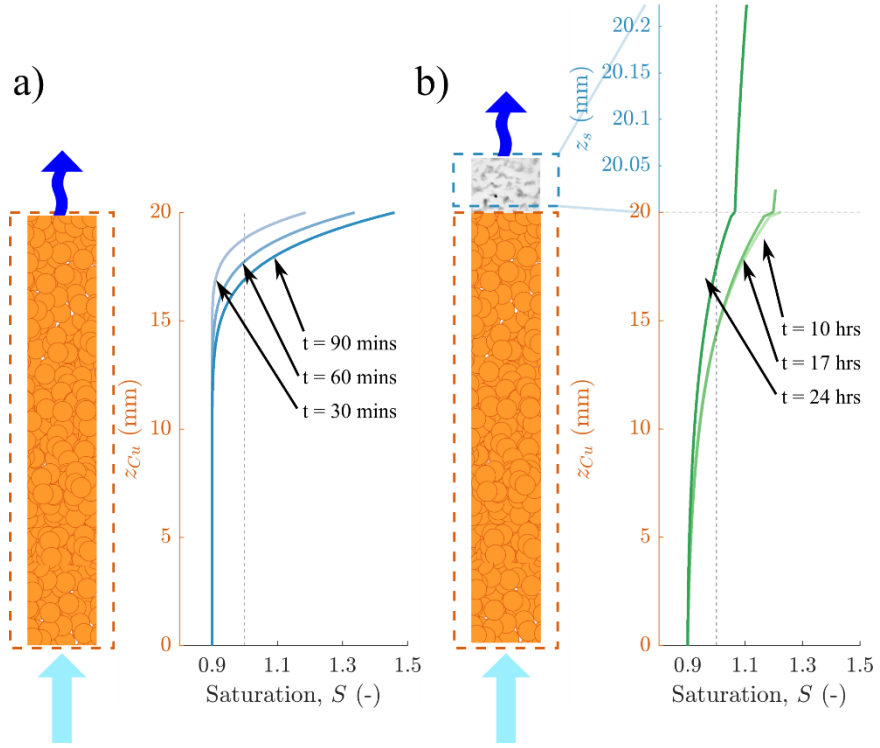

Figure 2. Saturation profiles of the salt solution a) at t = 30 min, 60 min, and 90 min within the porous domain before crystallization begins and b) at t = 10 hr, 17 hr, and 24 hr within the porous and salt crust domains after the onset of crystallization. [1.5 columns wide]

Figure 2 a) shows the saturation profiles inside the porous domain before the onset of crystallization. The profiles are shown at increasing times (t = 30 min, 60 min, and 90 min). At any instant, the saturation profile inside the medium increases monotonically as z_p varies from 0 to L_p. While only a single case is shown here, the shape of this curve is dictated by the Pe number. A higher Pe number implies that the advection affect is stronger (or diffusion effect lower) and results in a sharper gradient close to $z_p = L_p$. Conversely, a stronger diffusion effect smears out the saturation profile and makes the gradient more gradual. The mass fraction, and hence the saturation, within the porous domain increases

over time driven by evaporation. Once the saturation at $z_p = L_p$ reaches the critical supersaturation value of 1.6, crystallization initiates in the medium and the calculations transition to post-crystallization stage.

Saturation profiles within the porous medium and the salt crust domains are shown in Figure 2 b) at t = 10 hr, 17 hr, and 24 hr. Contrary to the pre-crystallization stage, saturation decreases in this stage. In the post-crystallization stage, the local saturation is governed by complicated interactions of advection, diffusion, and salt precipitation. Advection increases the local salt mass fraction. On the other hand, diffusion transports ions away from a higher saturation region and hence reduces the local salt mass fraction and smears out the local gradients. Precipitation of salt acts as a sink for the salt ions and reduces the saturation locally. The reaction term is active in a region close to $z_p = L_p$ within the porous medium domain (causing subflorescence) and the salt crust domain (causing efflorescence). Precipitation in turn dictates the local saturation and hence the above-mentioned regions are of interest (viz., close to $z_p = L_p$ within the porous medium and the salt crust domain, where precipitation occurs). With the onset of crystallization, the precipitation term is activated and acts as an ion sink. Precipitation occurs in the form of efflorescence as well as subflorescence, both increasing with time after the onset of crystallization. Diffusion, in conjunction with precipitation, overpowers the replenishment of ions by advection and reduces the local saturation. This can be seen in Figure 2 b) where the saturation curves inside the porous medium and salt crust domains shift to lower saturation values with increasing time. The strength of the diffusive term also reduces within the porous medium on account of the decreasing gradient. The decreasing saturation in turn decreases the rate of precipitation since it is proportional to (w-w_{sat}). This self-limiting behavior is expected to eventually drive the saturation profile towards a steady state. It is worth noting that the predicted salt mass fractions within the effloresced salt are relatively high (e.g. ~ 1.2 at 10 and 17 hr for the case shown in Figure 2) compared to the solubility limit. This is likely a result of the relatively low value of the reaction coefficient (1 μm/s) and the relatively high critical supersaturation (1.6) considered in this work.

Three cases with different *Pe* of 1.64, 2.32 and 3.55 (all with a fixed S_0 = 0.9) are run for an extended period of time (t = 50 hr) to observe the saturation profiles inside the porous domain, the growth of salt crust, and the amount of subflorescence. Figure 3 a) shows the saturation profiles inside the porous domain from t = 40 hr to t = 50 hr. The shaded regions corresponding to each *Pe* represent the variation of the corresponding saturation curves starting from t = 40 hr (shown by a solid line at the right edge) to t = 50 hr (solid line at the left edge). The reaction term from equation (8) is active only within the red-shaded region from z_p = 19.6 mm to $z_p = L_p$ = 20 mm, which shows the depth to which subflorescence is predicted to occur inside the porous domain. This region is hereafter referred to as the subflorescence zone. The inset shows a magnified view of the green boxed region. A sharp change in the gradient of the saturation profile can be observed for the case of *Pe* = 1.64 within the subflorescence zone, which can be attributed to the fact that the governing equation (equation (8)) is solved with the reaction term inside the subflorescence zone, but this reaction term is omitted outside this zone. The advective flux is the same in and outside the subflorescence zone and therefore the diffusive flux (and hence the gradient of the saturation profile) has a mismatch. Figure 3 b) and Figure 3 c) respectively show the evolution of the salt crust length and the amount of subflorescence with time for the three cases.

As expected, crystallization starts earlier with increasing *Pe* (at t = 10.3 hr, 5 hr, and 2.1 hr for *Pe* = 1.64, 2.32 and 3.55, respectively), as is evident from Figure 3 b). The salt crust length always increases thereafter. Saturation values within the majority of the salt crust length remain above S = 1 (similar to the behavior shown in Figure 2 b)) and hence precipitation increases the crust length. The growth of subflorescence shown in Figure 3 c) is, however, not monotonic and can be explained by looking closely at the saturation profiles within the porous domain. As shown in Figure 3 a), the shaded region, which represents the variation of the saturation curve in time, is wide for *Pe* = 1.64 and 2.32, and narrow for *Pe* = 3.55, implying that the saturation curve is very close to a steady state for *Pe* = 3.55 but not so for *Pe* = 1.64 and 2.32. The saturation inside the porous domain is higher than 1 for the case of *Pe* = 1.64 at all the times shown, which implies that the difference $(w\text{-}w_{sat}) > 0$, and hence only precipitation occurs.

This can be seen in Figure 3 c) where the line for *Pe* = 1.64 shows that the amount of subflorescence increases with time. This rate of increase, however, decreases on account of the reducing saturation inside the subflorescence zone. For the case of *Pe* = 2.32, the saturation profile is greater than 1 everywhere inside the subflorescence zone at t = 40 hr, but it falls below 1 before t = 50 hr. In contrast to *Pe* = 1.64, this implies that $(w\text{-}w_{sat}) < 0$ and the precipitated salt starts dissolving in the subflorescence zone, reducing the amount of subfloresced salt. This effect is more prominent for the case of *Pe* = 3.55, where $(w\text{-}w_{sat}) < 0$ in the subflorescence zone from t = 40 hr to t = 50 hr and the amount of subflorescence (line corresponding to *Pe* = 3.55 in Figure 3 c)) decreases over time.

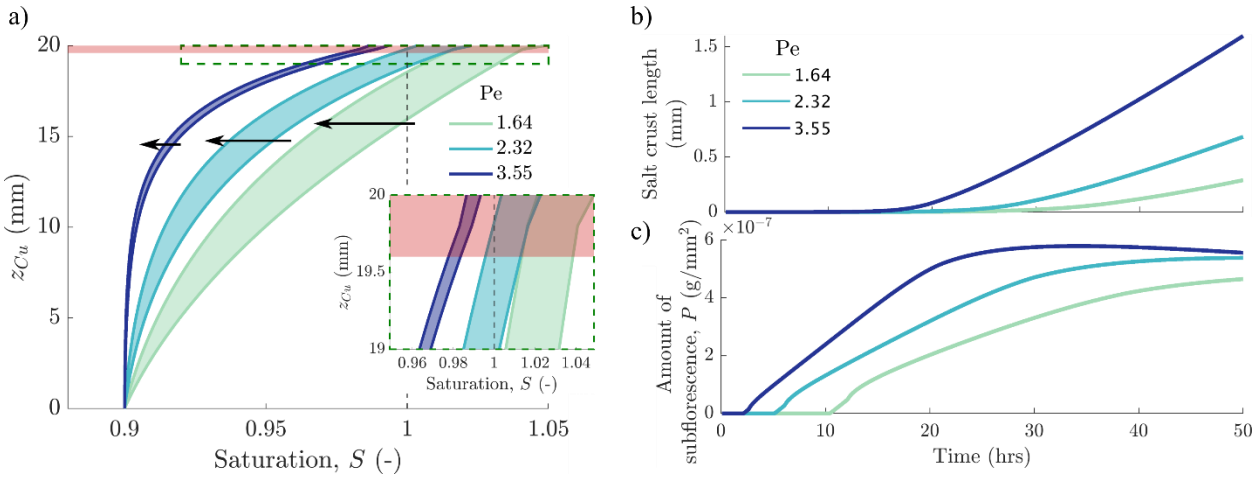

Figure 3. a) Saturation profiles inside the porous domain from t = 40 hr to t = 50 hr for three *Pe* numbers with the arrow showing the direction of time and the solid lines at the right and left edges of the shaded regions showing the profiles at t = 40 hr and t = 50 hr, respectively. The region in the green box is magnified and shown in the inset. The red-shaded region shows the depth to which subflorescence is predicted to occur. Evolution of b) salt crust length and c) the amount of subflorescence per unit cross-sectional area with time at the three *Pe* numbers. The source saturation is S_0 = 0.9 for all the cases. [2 columns wide]

The amount of precipitation per unit cross-sectional area inside the porous domain at the end of a 24 hr time period is calculated for several cases spanning a range of *Pe* numbers from 0.28 to 3.55 and

source saturations, S_0, from 0.1 to 0.9. The results are presented in the form of a grayscale contour plot in Figure 4, with darker shades representing higher amounts of precipitation. The solid blue curve represents the threshold *Pe* as predicted by equation (7). For combinations of *Pe* and S_0 below the blue curve, steady state is achieved before any crystallization occurs in the medium. On the other hand, crystallization, both as efflorescence and subflorescence occurring simultaneously, would be observed only for combinations of *Pe* and S_0 above and to the right of this blue curve. Combinations of *Pe* and S_0, close to the blue curve but above it, require more than 24 hr to observe any crystallization which explains the white region above the blue curve. The amount of subflorescence increases with increasing *Pe* and S_0 which is evident by the increasing darkness of the shade towards the top-right corner of the plot. Markers for the experimental cases (to be discussed later in Section 3) are also indicated in the plot.

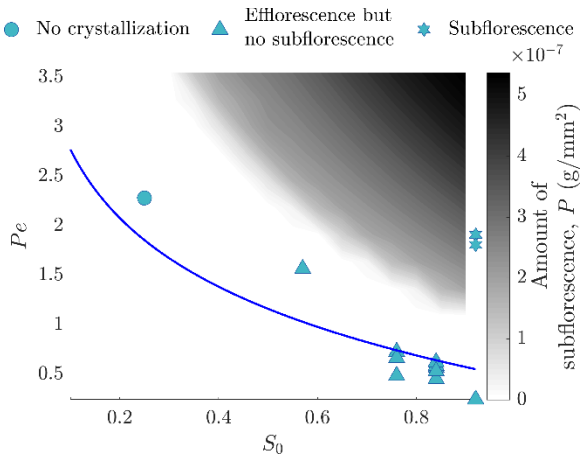

Figure 4. Contour plot showing the amount of precipitation per unit cross-sectional area inside the porous domain after t = 24 hr as a function of the *Pe* and the saturation of the source of salt solution (S_0). The markers indicate the observations of the evaporation experiments (circle for no crystallization, triangle for efflorescence but no subflorescence, and star for efflorescence and subflorescence), performed on copper particle porous media. [1 column wide]

The numerical model developed here has the capability to predict the saturation profiles within the porous domain as well as the effloresced salt crust domain. In addition to predicting the spatial

distribution of mass fraction and its temporal evolution in both the domains, a critical utility of the modeling framework is the ability to predict precipitation in the medium, both in the form of efflorescence and subflorescence, as well as the rates at which they occur. This model thus offers a unique capability to comprehensively study the process of evaporation-driven transport of solute in a porous medium.

3 EXPERIMENTS

Experiments are performed to mimic the domain and boundary conditions considered in the model. To first summarize the experimental approach, a porous medium is prepared by filling copper particles into a microchannel. This particle column is continually fed by a saline source of a known concentration from the bottom. Evaporation from the top surface drives the flow of the saline solution through the porous medium. The rate of evaporation is calculated by measuring the amount of water lost to the ambient via evaporation. The occurrence of any precipitation in the particle column (efflorescence and subflorescence) is observed visually. The dependence of subflorescence on the evaporation rate and source saturation is studied for comparison to the model.

A saline solution is prepared by adding anhydrous sodium chloride (Sigma-Aldrich®) to deionized (DI) water and magnetically stirring the mixture for 30 min. The saturation of the solution is controlled by controlling the amount of sodium chloride added. Multiple solutions of varying saturations are prepared and used as saline sources. The porous medium is comprised of copper particles in the size ranges of 180-212 μm or 90-106 μm. The particles are rendered hydrophilic by first cleaning with dilute HCl (1:2 by volume in DI water) for 30 s followed by oxidation in an alkaline solution (2 M NaOH and 0.1 M $(NH_4)_2S_2O_8$) for 1 hr and drying by heating in an oven set at 200 °C for 1 hr. The hydrophilic copper particles are then packed inside a glass microchannel of 2 mm inner diameter, resulting in a column diameter to particle diameter ratio of ~10 or 20. Spatial variations of variables across any cross-section can therefore be neglected and the transport processes can be assumed to be one-dimensional

along the length of the particle column. The porosity of the packed copper particles is measured separately as 0.65 (see Section S4 of the Supporting Information). The bottom end of the vertically oriented microchannel is capped with a filter paper (Whatman® Grade 1) held in place by an O-ring (2.2 mm inner diameter) as shown in the magnified view in Figure 5a). The filter paper prevents the copper particles from falling out but is permeable for the salt solution to pass through. The microchannel is suspended by passing it through a tapered rubber plug which seals into a test tube (16 mm diameter) filled with NaCl solution such that the lower end of the microchannel is immersed in the solution.

The test tube assembly is placed on top of a weighing balance (Sartorius Entris™ II Essential Analytical Balance). The weight is recorded every 5 min while simultaneously imaging the channel from the top using a high-magnification lens (VH-Z100R, Keyence) attached to a CCD camera (EO-5023M 2/3" Monochrome, Edmund Optics), as well as from the side by a different lens (50 mm f/1.7 prime lens, Minolta augmented by a 2x Macro Focusing Teleconverter, Vivitar) and CCD camera (EO-1312M 1/2" Monochrome, Edmund Optics) as shown in Figure 5 a). The relative humidity and temperature of the ambient close to the open top mouth of the microchannel are measured at the start of each experiment using a humidity/temperature meter (OMEGA RHXL3SD). Each experiment consists of allowing evaporation from the top of the microchannel to the ambient for a period of 24 hr, after which the rubber plug is removed from the test tube and transferred to a Styrofoam holder, and the channel is imaged from

the side using a DSLR camera (D5200, Nikon) and the high-magnification lens (VH-Z100R, Keyence) to check for any presence of subflorescence; this post-test imaging setup is shown in Figure 5 b).

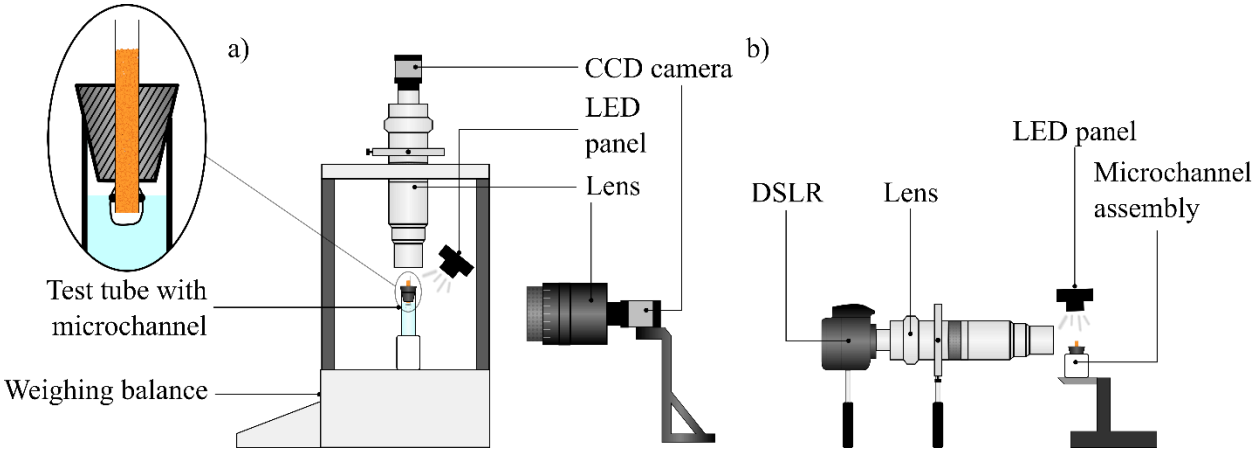

Figure 5. Schematic diagram describing the experimental setup for a) characterizing the evaporation rate and observing the particle column from the top and the side and b) checking for presence of subflorescence after the test. [2 columns wide]

The top-view lens is focused on the top surface of the copper particle column from which water evaporates to the ambient. The onset of crystallization and the subsequent growth of efflorescence is captured in this view. The side-view imaging during the evaporation test is performed only for general monitoring of the evaporation process. The cumulative water lost via evaporation at any instant of time during the test is calculated as the difference between the initial weight and the weight recorded at that instant.

Multiple experiments were performed by changing the source saturation while the ambient air was fairly invariant with a temperature of 22.5±0.5 °C and a relative humidity of 35.7±1.0 % close to the mouth of the microchannel. Evaporation occurs naturally from the top of the microchannel and its flux was not a controlled parameter. However, the height of the copper particle column and hence the distance between the top of the column and the top of the microchannel was slightly different between the cases and caused different evaporation fluxes to be observed. It is also important to note that in many of the

experiments, a salt crust formed on the side walls of the microchannel above the top surface of the particle column. Salt solution wicking into the porous salt crust on the side walls induces additional evaporation and would cause significant deviation from the one-dimensional behavior that is sought. Hence, any test cases with significant side wall crystallization as observed from the side-view visualizations are discarded.

The results from a representative evaporation test are shown in Figure 6. The mass fraction of the salt solution source is 0.222 which corresponds to a saturation of $S_0 = 0.84$, the length of the copper particle column is ~ 23 mm, and the associated *Pe* number is 0.53. Figure 6 a) plots the evaporated mass against time, with symbols marking the mass at times of 2 hr, 12.5 hr, and 20 hr from the start of the experiment corresponding to the top-view images of the particle column shown in Figure 6 b). Two hours into the test, the particles are clearly visible along with the salt solution, evidenced by the glistening reflections from the liquid-vapor interfaces. A salt crust forms on the top surface starting at ~ 8 hr. The glistening effect is no longer visible once the salt forms a crust over the entire top surface, as in the top-view image at 12.5 hr. The effloresced salt is prominently visible near the end of the experiment in the image from 20 hr. The mean evaporation rate is extracted by fitting a linear model to the evaporated mass over the time period of interest. The mean evaporation flux is initially higher (4.39×10^{-5} kg/m^{2}s from $t = 0$ to $t \approx 8$ hr), but reduces to 1.69×10^{-5} kg/m^{2}s from $t \approx 8$ hr to $t = 24$ hr. This reduction is coincident with the initiation of efflorescence and happens invariably for all the cases tested. We speculate that the evaporation rate decreases due to efflorescence forming a crust over the entire evaporating surface, an effect which has been documented in the literature [26,41]. Subflorescence, if it were to occur, would begin only after the onset of crystallization within the copper particle column near the top evaporating surface. The lower mean evaporation rate calculated for the later portion of the experiment after crystallization is thus of interest with respect to the formation of subflorescence; hence the *Pe* numbers of the experiments shown on the contour plot in Figure 4 are calculated using these lower evaporation rates.

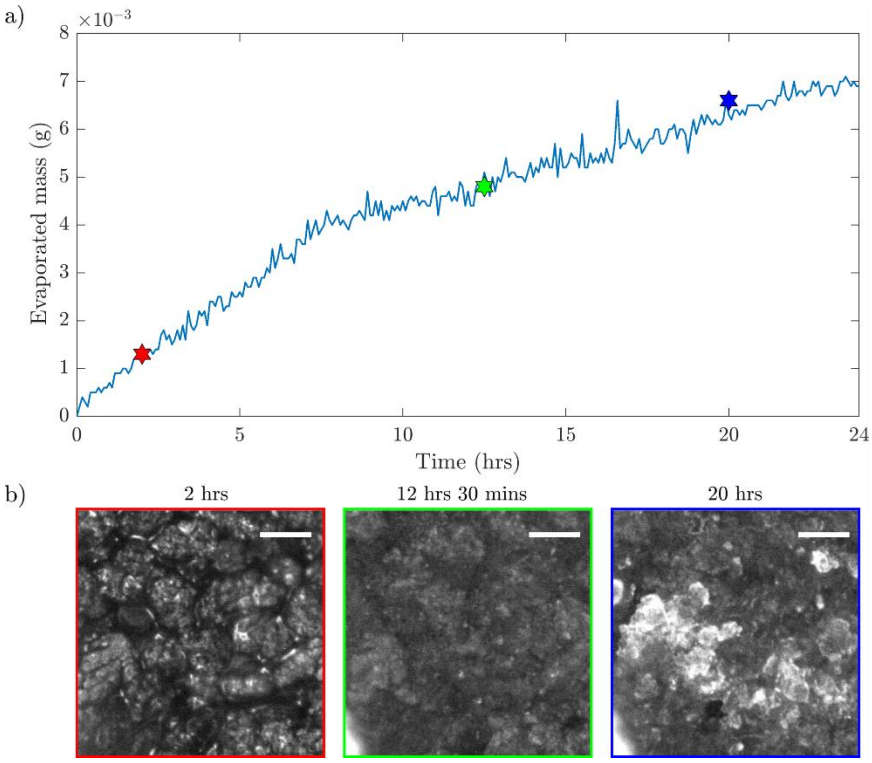

Figure 6. a) Mass of water evaporated during a period of 24 hr from a copper particle column connected to a salt solution source at a saturation S_0 = 0.84. b) Top-view images of the particle column at three instants showing the particles with no efflorescence at 2 hr and with efflorescence at 12.5 hr and 20 hr. The scale bar in each image represents 100 µm. [1.5 column wide]

The side-view imaging using the DSLR camera is performed post-test to explore for the presence of subflorescence. Figure 7 shows the side-view photographs side-by-side with schematics for test cases with a solution source saturation of S_0 = 0.92 at two *Pe* numbers of a) 0.23 and b) 1.96. Efflorescence occurs but without any noticeable subflorescence for the lower *Pe* case, as a clear distinction can be seen between the copper particles in the lower part of the image and the effloresced white salt crust on top. Both efflorescence and subflorescence are observed for the higher *Pe* case. The solid white region in the top portion of the image shows the effloresced salt crust, while the copper particles below have embedded subfloresced salt. These regions are also depicted in the accompanying schematics, where the copper particles are shown along with the crystalline precipitated salt.

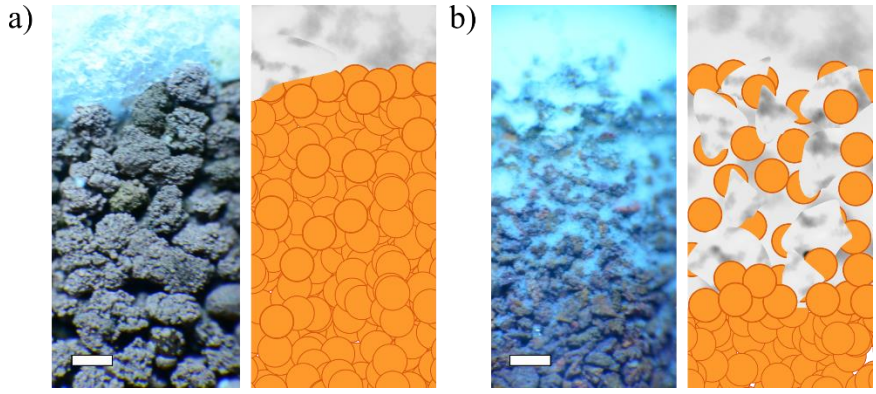

Figure 7. Side-view images of the copper particle domain viewing the top of the column after t = 24 hr corresponding to experiments conducted by using a solution source saturation of S_0 = 0.92 at *Pe* numbers of a) 0.23, showing efflorescence without subflorescence and b) 1.96, showing efflorescence along with subflorescence, accompanied by schematics showing the copper particle domain and the crystallized salt. The scale bar in the photographs represents 200 μm. [1.5 columns wide]

All of the test cases performed were classified based on the observation of the type of crystallization from the side-view images as having i) no crystallization, ii) efflorescence, but no subflorescence, or iii) both efflorescence and subflorescence. The *Pe* and S_0 of the test cases along with the observation of the type of crystallization is depicted by markers in Figure 4. As predicted by the numerical model, only efflorescence is observed when the *Pe* is not high enough, for solution source saturations of S_0 = 0.57, 0.76, 0.84 and 0.92 (shown by the triangular markers). At higher *Pe* numbers for S_0 = 0.92, subflorescence is observed in addition to efflorescence (star markers). We also observe steady-state evaporation without any precipitation inside the medium for S_0 = 0.25 and *Pe* = 2.28 (circular marker). The primary trend predicted by the numerical model, viz., the amount of subflorescence within the medium increases with higher S_0 and *Pe* values, is observed in our experiments as well. We note, however, that the purpose of the experiments is not to validate the numerical predictions, but to merely confirm the trends predicted by the model.

We offer the model developed here as a comprehensive tool to evaluate the mass fraction profiles within a porous medium subject to evaporation. The primary capabilities of the model are to: i) evaluate the solute saturation profile within the porous medium and the effloresced salt crust, ii) predict the growth rate of efflorescence, and iii) predict the amount of subflorescence within the porous medium. The model uses parametric values such as reaction coefficient, salt crust porosity, critical supersaturation, and diffusion coefficient from the literature. A wide range of values have been reported for some of these parameters such as the reaction coefficient and the critical supersaturation, and hence the accuracy of the model predictions is intrinsically tied to the accuracy to which these values can be specified. The system behavior depends strongly on these parameters, as discussed in Section S4 of the Supporting Information, and thus without accurate *a priori* knowledge of these parameters, a direct validation of the model against the experiments is not possible. The predictive capabilities of the model will thus benefit as these parameters become available with more precision and a validation can be performed with appropriate experiments.

4 CONCLUSIONS

The dynamics of salt crystallization driven by evaporation of a salt solution from a porous medium has been investigated. A comprehensive model is developed to predict the mass fraction profiles inside a porous medium by solving the transient advection-diffusion equation with an accounting of precipitation and dissolution of salt after the local saturation exceeds critical supersaturation. This approach further offers the unique capabilities of predicting the mass fraction profile inside the effloresced salt crust which allows a calculation of salt crust growth rate, as well as calculation of the amount of precipitation inside the porous medium – a direct measure of subflorescence. The dynamics of salt crystallization is shown to be a strong function of the saturation of the salt solution source and *Pe* of flow within the medium (determined by the evaporation flux). Temporal evolution of the saturation profiles, the salt crust length, and the amount of subflorescence inside the medium are analyzed. It is observed that for higher *Pe* the saturation profile within the porous medium reaches a steady state. The salt crust length keeps increasing

due to continuous efflorescence for all the *Pe* number cases investigated, while the amount of subflorescence first increases but can later decrease when the solute saturation inside the porous medium reaches sub-saturation values. Experiments are conducted to check the subflorescence trends predicted by the model. To mimic the boundary conditions of the model, a microchannel filled with copper particles is connected to a source of salt solution and is allowed to evaporate to the ambient from the open top of the particle column. Experiments were performed to observe cases with i) no crystallization, ii) efflorescence without subflorescence, and iii) efflorescence and subflorescence. The expected trend of observing subflorescence with increasing source saturation, S_0, and *Pe* is experimentally verified. With calibration of the necessary model inputs, this approach can be broadly utilized as a predictive tool for solute transport and precipitation in porous media driven by evaporation.

AUTHOR INFORMATION

Corresponding Author

*E-mail: jaweibel@purdue.edu

Notes

The authors declare no competing financial interest.

5 REFERENCES

[1] C. Rodriguez-Navarro, E. Doehne, Salt weathering: influence of evaporation rate, supersaturation and crystallization pattern, Earth Surf. Process. Landforms. 24 (1999) 191–209.

[2] N. Shahidzadeh-Bonn, J. Desarnaud, F. Bertrand, X. Chateau, D. Bonn, Damage in porous media due to salt crystallization, Phys. Rev. E. 81 (2010) 066110.

[3] G.W. Scherer, Stress from crystallization of salt, Cem. Concr. Res. 34 (2004) 1613–1624.

[4] H.W. Wellman, A.T. Wilson, Salt weathering, a neglected geological erosive agent in coastal and arid environments, Nature. 205 (1965) 1097–1098.

[5] T. Hosono, E. Uchida, C. Suda, A. Ueno, T. Nakagawa, Salt weathering of sandstone at the Angkor monuments, Cambodia: identification of the origins of salts using sulfur and strontium isotopes, J. Archaeol. Sci. 33 (2006) 1541–1551.

[6] N. Kuchitsu, T. Ishizaki, T. Nishiura, Salt weathering of the brick monuments in Ayutthaya, Thailand, Eng. Geol. 55 (2000) 91–99.

[7] B. Fitzner, K. Heinrichs, D. La Bouchardiere, Limestone weathering of historical monuments in Cairo, Egypt, Geol. Soc. London, Spec. Publ. 205 (2002) 217–239.

[8] S. Dai, H. Shin, J.C. Santamarina, Formation and development of salt crusts on soil surfaces, Acta Geotech. 11 (2016) 1103–1109.

[9] H. Pathak, D.L.N. Rao, Carbon and nitrogen mineralization from added organic matter in saline and alkali soils, Soil Biol. Biochem. 30 (1998) 695–702.

[10] V.N.L. Wong, R.C. Dalal, R.S.B. Greene, Salinity and sodicity effects on respiration and microbial biomass of soil, Biol. Fertil. Soils. 44 (2008) 943–953.

[11] A. Lekhal, B.J. Glasser, J.G. Khinast, Impact of drying on the catalyst profile in supported impregnation catalysts, Chem. Eng. Sci. 56 (2001) 4473–4487.

[12] M. Börnhorst, P. Walzel, A. Rahimi, A. Kharaghani, E. Tsotsas, N. Nestle, A. Besser, F. Kleine Jäger, T. Metzger, Influence of pore structure and impregnation–drying conditions on the solid distribution in porous support materials, Dry. Technol. 34 (2016) 1964–1978.

[13] Y. Ito, Y. Tanabe, J. Han, T. Fujita, K. Tanigaki, M. Chen, Multifunctional porous graphene for high-efficiency steam generation by heat localization., Adv. Mater. 27 (2015) 4302–7.

[14] Y. Li, T. Gao, Z. Yang, C. Chen, W. Luo, J. Song, E. Hitz, C. Jia, Y. Zhou, B. Liu, B. Yang, L. Hu, 3D-printed, all-in-one evaporator for high-efficiency solar steam generation under 1 sun illumination., Adv. Mater. 29 (2017) 1700981.

[15] C. Chang, P. Tao, B. Fu, J. Xu, C. Song, J. Wu, W. Shang, T. Deng, Three-dimensional porous solar-driven interfacial evaporator for high-efficiency steam generation under low solar flux, ACS Omega. 4 (2019) 3546–3555.

[16] H.T. El-Dessouky, H.M. Ettouney, Multiple effect evaporation, Fundam. Salt Water Desalin., (2002) 147–208.

[17] H.T. El-Dessouky, H.M. Ettouney, Multiple-effect evaporation desalination systems: thermal analysis, Desalination. 125 (1999) 259–276.

[18] S. He, C. Chen, Y. Kuang, R. Mi, Y. Liu, Y. Pei, W. Kong, W. Gan, H. Xie, E. Hitz, C. Jia, X. Chen, A. Gong, J. Liao, J. Li, Z.J. Ren, B. Yang, S. Das, L. Hu, Nature-inspired salt resistant bimodal porous solar evaporator for efficient and stable water desalination, Energy Environ. Sci. 12 (2019) 1558–1567.

[19] P. Qiu, F. Liu, C. Xu, H. Chen, F. Jiang, Y. Li, Z. Guo, Porous three-dimensional carbon foams with interconnected microchannels for high-efficiency solar-to-vapor conversion and desalination, J. Mater. Chem. A. 7 (2019) 13036–13042.

[20] X. Wang, M.L. Hsieh, J.A. Bur, S.Y. Lin, S. Narayanan, Capillary-driven solar-thermal water desalination using a porous selective absorber, Mater. Today Energy. 17 (2020) 100453.

[21] A.R.A. Elbar, H. Hassan, Enhancement of hybrid solar desalination system composed of solar panel and solar still by using porous material and saline water preheating, Sol. Energy. 204 (2020) 382–394.

[22] X. Han, L. Zang, S. Zhang, T. Dou, L. Li, J. Yang, L. Sun, Y. Zhang, C. Wang, Hydrophilic

polymer-stabilized porous composite membrane for water evaporation and solar desalination, RSC Adv. 10 (2020) 2507–2512.

[23] M. Rey, F. Lauro, Ocean thermal energy and desalination, Desalination. 39 (1981) 159–168.

[24] R. Lazhar, M. Najjari, M. Prat, Combined wicking and evaporation of NaCl solution with efflorescence formation: The efflorescence exclusion zone, Phys. Fluids. 32 (2020) 067106.

[25] U. Nachshon, N. Weisbrod, Beyond the salt crust: on combined evaporation and subflorescent salt precipitation in porous media, Transp. Porous Media. 110 (2015) 295–310.

[26] S. Veran-Tissoires, M. Prat, Evaporation of a sodium chloride solution from a saturated porous medium with efflorescence formation, J. Fluid Mech. 749 (2014) 701–749.

[27] S. Veran-Tissoires, M. Marcoux, M. Prat, Discrete salt crystallization at the surface of a porous medium, Phys. Rev. Lett. 108 (2012) 3–6.

[28] S. Veran-Tissoires, M. Marcoux, M. Prat, Salt crystallisation at the surface of a heterogeneous porous medium, EPL. 98 (2012) 34005.

[29] M.N. Rad, N. Shokri, A. Keshmiri, P.J. Withers, Effects of grain and pore size on salt precipitation during evaporation from porous media, Transp. Porous Media. 110 (2015) 281–294.

[30] N. Sghaier, S. Geoffroy, M. Prat, H. Eloukabi, S. Ben Nasrallah, Evaporation-driven growth of large crystallized salt structures in a porous medium, Phys. Rev. E. 90 (2014) 042402.

[31] M. Norouzi Rad, N. Shokri, M. Sahimi, Pore-scale dynamics of salt precipitation in drying porous media, Phys. Rev. E. 88 (2013) 032404.

[32] N. Shokri, Pore-scale dynamics of salt transport and distribution in drying porous media, Phys. Fluids. 26 (2014) 012106.

[33] L. Guglielmini, A. Gontcharov, A.J. Aldykiewicz, H.A. Stone, Drying of salt solutions in porous

materials: Intermediate-time dynamics and efflorescence, Phys. Fluids. 20 (2008) 077101.

[34] G. Licsandru, C. Noiriel, P. Duru, S. Geoffroy, A. Abou Chakra, M. Prat, Dissolution-precipitation-driven upward migration of a salt crust, Phys. Rev. E. 100 (2019) 032802.

[35] H. Dashtian, N. Shokri, M. Sahimi, Pore-network model of evaporation-induced salt precipitation in porous media: The effect of correlations and heterogeneity, Adv. Water Resour. 112 (2018) 59–71.

[36] F. Ahmad, A. Rahimi, E. Tsotsas, M. Prat, A. Kharaghani, From micro-scale to macro-scale modeling of solute transport in drying capillary porous media, Int. J. Heat Mass Transf. 165 (2021) 120722.

[37] L. Shen, Z. Chen, Critical review of the impact of tortuosity on diffusion, Chem. Eng. Sci. 62 (2007) 3748–3755.

[38] J. Desarnaud, H. Derluyn, J. Carmeliet, D. Bonn, N. Shahidzadeh, Metastability limit for the nucleation of NaCl crystals in confinement, J. Phys. Chem. Lett. 5 (2014) 890–895.

[39] J. Desarnaud, H. Derluyn, J. Carmeliet, D. Bonn, N. Shahidzadeh, Hopper growth of salt crystals, J. Phys. Chem. Lett. 9 (2018) 2961–2966.

[40] J.A. Weibel, S. V. Garimella, M.T. North, Characterization of evaporation and boiling from sintered powder wicks fed by capillary action, Int. J. Heat Mass Transf. 53 (2010) 4204–4215.

[41] H. Eloukabi, N. Sghaier, S. Ben Nasrallah, M. Prat, Experimental study of the effect of sodium chloride on drying of porous media: The crusty–patchy efflorescence transition, Int. J. Heat Mass Transf. 56 (2013) 80–93.